Rotor Wake Modeling for Mars Rotorcraft using the Viscous Vortex Particle Method

Tove Ågren
Aerospace Engineer
Analytical Mechanics Associates
NASA Ames Research Center
Moffett Field, CA, U.S.A.

Nicholas Peters
Aerospace Engineer
NASA Ames Research Center
Moffett Field, CA, U.S.A.

Allen Ruan
Aerospace Engineer
Analytical Mechanics Associates
NASA Ames Research Center
Moffett Field, CA, U.S.A.

ABSTRACT

The next generation of Mars rotorcraft may involve an increase in scale and number of rotors. A key focus area that has been identified is to increase the fidelity of rotor wake modeling, including its impact on flight dynamics. To that end, this paper pursues the use of a Viscous Vortex Particle Method (VVPM) for mid-fidelity rotor wake predictions in Mars atmospheric conditions. Simulated aerodynamic hover performance, as well as control efforts in trimmed forward flight, of the Ingenuity Mars Helicopter with a VVPM wake is shown to correlate well with available experimental data. Qualitative and quantitative coaxial wake effects for Ingenuity-type rotors in hover and forward flight as predicted with VVPM are studied. Utilizing VVPM to evaluate rotor-rotor interference effects in a large-scale Mars hexacopter across a wide range of flight conditions showcases the capability to comprehensively model the induced wake of complex multi-rotor configurations within feasible computational cost. An approach to emulate interference effects derived from the VVPM data that is compatible with finite-state dynamic inflow models is demonstrated, exemplifying how VVPM can be adopted to inform flight dynamics analysis and control system design of next-generation Mars rotorcraft.

NOTATION

a	Speed of sound, m/s
A	Rotor disk area, m^2
C_P	Rotor power coefficient, $P/(\rho A(\Omega R)^3)$
C_T	Rotor thrust coefficient, $T/(\rho A(\Omega R)^2)$
C_{F_z}	Rotor vertical force coefficient, $F_z/(\rho A(\Omega R)^2)$
$c_{.75}$	Chord at 0.75R, m
d	Coaxial rotor separation, m
F_z	Vertical rotor hub force, N
FM	Hover figure of merit, $T\sqrt{T/(2\rho A)}/P$
M	Interference gain matrix
M_{tip}	Blade tip Mach number
N_b	Number of blades
N_r	Number of rotors
P	Rotorcraft power, W
r	R otor radial coordinate, m
R	Gas constant, m^2/(s^{2}K); rotor radius, m
Re	Chord-based Reynolds number, $\rho V c/\mu$
RPM	Rotor rotational speed, rev/min
t	Time, s
T	Temperature, K; rotor thrust, N
$\mathbf{u}$	Velocity field, m/s
V	Airspeed, m/s
v_i	Induced velocity, m/s
x_i	Position of vorticity particle i, m
$\boldsymbol{\alpha}$	Vortex particle vorticity vector
α	Angle of attack, deg
λ_i	Dimensionless induced velocity, $v_i/(\Omega R)$
γ	Specific heat ratio; flight path angle, deg
μ	Dynamic viscosity, N·s/m^2; advance ratio
ν	Kinematic viscosity, μ/ρ
ψ	Rotor azimuth angle, deg
ρ	Density, kg/m^3
σ	Rotor solidity (thrust-weighted)
θ_0	Rotor collective angle, deg
θ_c, θ_s	Rotor cosine and sine cyclic, deg
Ω	Rotor rotational speed, rad/s
$\boldsymbol{\omega}$	Vorticity field, 1/s
ξ	Particle distribution function

Sub- and superscripts

ind	Self-induced
$intf$	Interference
u, l	Upper and lower rotor
h, v	Horizontal and vertical
σ	Smoothing parameter

INTRODUCTION

The success of the Ingenuity Mars Helicopter has broadened the scope of extraterrestrial vertical take-off and landing (VTOL) capabilities. Extensive modeling, simulation, and experimental testing efforts preceding take-off on Mars were undertaken in order to bring to fruition Ingenuity's success.

Presented at the Vertical Flight Society's 81st Annual Forum & Technology Display, Virginia Beach, VA, USA, May 20–22, 2025.

Capturing the effects of the induced rotor wake on both aerodynamic performance and flight dynamics was critical for an accurate model development of Ingenuity, and will be of even greater importance as more complex, multi-rotor, and hybrid vehicle concepts are currently being proposed for Martian flight (Refs. 1–4). The reliance on model-based analysis for planetary rotorcraft highlights the need for high-fidelity solutions, as experimental validation is challenging, especially at forward flight speeds and large vehicle scales that are beyond capabilities of current testing facilities suited for Martian conditions (Ref. 5). The Mars environment presents a distinct challenge: aerodynamics and flight dynamics of a Mars helicopter differ markedly from those observed on Earth, stemming from the low atmospheric density and reduced gravity operating condition, and the resulting unique mechanical design requirements necessary for operating in such an environment (Refs. 6, 7). Numerically simulating rotorcraft in Martian conditions remains a challenging task, even with high-fidelity, blade-resolved Computational Fluid Dynamics (CFD) models, owing to the relatively unexplored flow regime of low Reynolds and high-subsonic Mach numbers (Ref. 8). The dynamic inflow model used for Ingenuity (Refs. 9, 10) is a simple, global representation of the rotor wake and its coupling with (low-frequency) rotor and bare-airframe dynamics (Ref. 11). While computationally tractable for real-time simulation and suitable for control system design, such models fail to capture higher-order rotor wake dynamics and do not explicitly nor a-priori model wake contraction, distortion, roll-up, rotor-wake interaction, or rotor-rotor interference effects. Experimental data on multi-rotor applications for the considered low Reynolds number is limited (Ref. 12), and even more so in the high sub-sonic aerodynamic regime, hindering semi-empirical formulations such as conventional prescribed or free wake approaches to solve for the wake convection and diffusion. Blade-resolved high-fidelity CFD can be used to achieve high-resolution numerical simulation of rotor wakes from first principles. However, reliance on blade-resolved CFD methods comes at a significant computational cost, which increases drastically with the number of rotors or aerodynamic surfaces. The identified gap in tools available for rotor-induced wake modeling for Mars rotorcraft underscores the need for a mid-fidelity approach that retains important higher-order features and wake interactional effects, while also being applicable to general multiple rotor and compound rotorcraft configurations within a viable computational cost.

The VVPM approach to rotor wake modeling has been shown to accurately capture unsteady rotor wake dynamics, including viscous effects, rotor-wake interaction and rotor-rotor interference in Earth-based multi-rotor configurations (Refs. 13–19). VVPM is also increasingly being acknowledged as a mid-fidelity tool from which reduced-order, state-space inflow models for flight dynamics analysis, control system design, and real-time simulations can be derived or enhanced (Refs. 20–22). While VVPM has recently gained attention as a computationally efficient method for modeling complex wake interactions in advanced rotorcraft concepts, little research has focused on validating and applying the method specifically to Mars rotorcraft. Unlike commonly used wake models for comprehensive analys that rely on potential flow assumptions, VVPM accommodates simulating the effect of air viscosity on physical vorticity diffusion throughout the entire flowfield, a feature that is arguably of particular interest for Mars applications, considering the dramatically reduced prevailing Reynolds number.

This paper aims to demonstrate the utility of VVPM as a mid-fidelity tool for Mars rotorcraft wake prediction, providing a bridge between simplified dynamic inflow models and grid-based high-fidelity CFD. The objective reads two-fold: first, validate the rotor wake prediction capabilities in the extreme aerodynamic flow regime the Mars environment poses. Second, utilize VVPM to analyze critical wake effects of current and future Mars rotorcraft configurations. After a brief description of the numerical approach, simulations of Ingenuity-type rotors with a VVPM wake is correlated against available experimental data in representative Mars atmospheric conditions, from vacuum chamber testing as well as select Mars flight data. Simulated coaxial interference effects and unsteady aerodynamic loading due to the rotor wake are studied. Moving towards the next generation of Mars rotorcraft, VVPM is used to study wake dynamics for Chopper, a proposed large scale hexacopter (Ref. 4). Rotor-rotor interference and its impact on trim, rotor loads and induced velocity distributions are presented for a range of flight conditions, focusing on the extremes of the flight envelope, including high speed forward flight. An approach to extract pairwise rotor-rotor interference velocities is demonstrated, for the purpose of deriving reduced-order surrogates of the VVPM simulation data that lend themselves to real-time flight dynamics models.

NUMERICAL APPROACH

VVPM is a first principles approach to modeling fluid dynamics, utilizing a Lagrangian description of the incompressible Navier-Stokes equation in its vorticity-velocity form. The implementation as embodied in the rotorcraft analysis tool FLIGHTLAB (Ref. 23) has been accounted for in detail in Refs. 13, 24. Let $d(\cdot)/dt = \partial(\cdot)/\partial t + \mathbf{u}\cdot\nabla(\cdot)$ denote the material derivative associated with a velocity field $\mathbf{u}$. For the vorticity field $\boldsymbol{\omega} = \nabla\times\mathbf{u}$ and kinematic viscosity ν, vorticity dynamics are governed by

$$\frac{d\boldsymbol{\omega}}{dt} = \boldsymbol{\omega}\cdot\nabla\mathbf{u} + \nu\Delta\boldsymbol{\omega}. \tag{1}$$

The implicit representation of convection in Equation (1) allows for a numerical solution without artificial dissipation as compared to traditional finite differencing and volume schemes. As such, VVPM more efficiently retains vortex circulation strenght over time. The vortex diffusion term $\nu\Delta\boldsymbol{\omega}$ is solved for based on Particle Strength Exchange techniques (Ref. 25), where the Laplacian operator Δ is approximated by an integral operator, avoiding numerical differentiation. Compared to grid-based CFD, the VVPM implementation in this

study is a grid-free approach. Instead, Equation (1) is discretized through a vortex particle ensemble representation of the vorticity field, giving the approximation

$$\tilde{\boldsymbol{\omega}}(x,t) = \sum_{i=1} \xi_\sigma(x - x_i)\boldsymbol{\alpha}_i \tag{2}$$

where $\boldsymbol{\alpha}_i$ is the total vorticity inside the i:th particle located at x_i, and ξ_σ is a distribution function parameterized with a smoothing parameter σ as to avoid a singularity representation and ensure convergence. The majority of implementations, including the scheme in FLIGHTLAB, assigns a Gaussian distribution to ξ_σ. While the VVPM wake model enjoys a formulation free from empirical tuning parameters (not including the rotor aerodynamic model itself), the numerical discretization and boundary conditions must be prescribed. To determine the appropriate simulation parameters, preliminary convergence and sensitivity studies to discretization resolution and boundary conditions were conducted and substantiated with prior studies (Refs. 19, 24). The final parameter bounds are tabulated in Table 1. Aerodynamic surfaces,

Table 1. VVPM Simulation Parameters.

Particle cut-off distance	$\leq 7R$
Max number of particles	8×10^6
Far-field boundary condition	≤ 15 rev.
Particle Resolution	$\geq 0.0025R$
Vorticity Source Resolution	$\geq 0.03R$

such as rotor blades, act as vorticity sources, shedding new vortex particles as lift is generated. The considered aerodynamic rotor blade model is based on lifting line theory with a Weissinger-L 3-D correction to model tip losses. No additional unsteady models for attached flow or dynamic stall is included. Non-linear effects of compressibility and viscosity on airfoil performance are accounted for through look-up tables of the sectional lift, drag and moment as function of angle of attack and Mach number. For varying atmospheric conditions (density and temperature), dedicated airfoil decks are used to ensure that the effects of Reynolds number are accurately captured. All airfoil look-up tables are derived from 2D CFD OVERFLOW simulations using current best practices for low Reynolds number high subsonic simulations. For a detailed account of the CFD modeling approach and assumptions, refer to Ref. 8. The rotor blades are assumed rigid, and flap dynamics are emulated with hinges, where stiffness and damping is tuned to match the physical fundamental flap mode.

THE INGENUITY MARS HELICOPTER

The coaxial rotor system of Ingenuity is modeled in FLIGHTLAB with a coupled VVPM wake to validate the prediction capabilities of rotor performance in aerodynamic conditions representative for Mars. Simulated performance metrics with VVPM are compared against available data in a range of atmospheric densities. Forward flight trim solutions from select Mars flight data are compared against VVPM predictions. In addition, the Ingenuity rotor system is studied in simulation to characterize coaxial interference and unsteady aerodynamic loads arising from wake effects.

Experimental Correlation to Ingenuity Hover Test Data

In support of the Ingenuity Mars Helicopter and Sample Recovery Helicopters (SRH) (Ref. 26), experimental aerodynamic performance tests were conducted in the NASA Jet Propulsion Laboratory 25 ft Space Simulator (JPL SS). The tests aimed to expand the capabilities of the Ingenuity rotor system to support increased liftoff mass. The test articles, experimental set-up, and data collection is covered at length in Refs. 27, 28. The coaxial rotor performance tests of the Engineering Development Model 1 (EDM-1) is considered herein for VVPM wake model validation. It is noted, that while the EDM-1 test campaign explored increased blade loading, C_T/σ, with the objective of characterizing stall and power limits, the nominal operating range of Ingenuity is of primary interest for test data correlation. The coaxial, two-bladed hingeless rotor system of EDM-1 is a very close replica to the flight vehicle, with the exception of an adjustment to the pitch links to accommodate larger collective pitch deflections. A global characterization of the rotor geometry is provided in Table 2, alongside the aerodynamic environment for the subset of tests replicated in simulation. Collective sweeps for

Table 2. Test Article and Conditions.

Rotor Characteristics	
Rotor radius, R [m]	0.605
Number of blades, N_b	4
Chord length at $.75R$, $c_{.75}$ [m]	0.074
Solidity, σ	0.148
Vertical rotor separation, d [m]	$\approx 0.17R$
Aerodynamic Conditions	
Temperature, T [K]	293
Gas constant, R [Nm/kg/K]	188.0
Specific heat ratio, γ	1.289
Dynamic viscosity, μ [Ns/m^2]	1.46×10^{-5}
Speed of sound, a [m/s]	267

Table 3. Test Matrix for EDM1 VVPM Correlation.

Case ID	**RPM**	**Density** (kg/m^3)	M_{tip}	**Re**
1	2200	0.0100	0.52	5254
2	2043	0.0185	0.48	8971
3	2550	0.0185	0.60	11230

rotor performance analysis were executed in the experiments ranging from 1° to 22.5° at a set of density and rotor tip speed combinations. For the purpose of prediction correlation with

VVPM, collective sweeps were simulated in equivalent conditions as the select test runs as tabulated in Table 3.

The coaxial rotor performance as predicted with the VVPM wake is compared to the experimental data, discussed as follow. Figure 1 shows the blade loading versus collective (Figure 1a) and power versus thrust (Figure 1b).

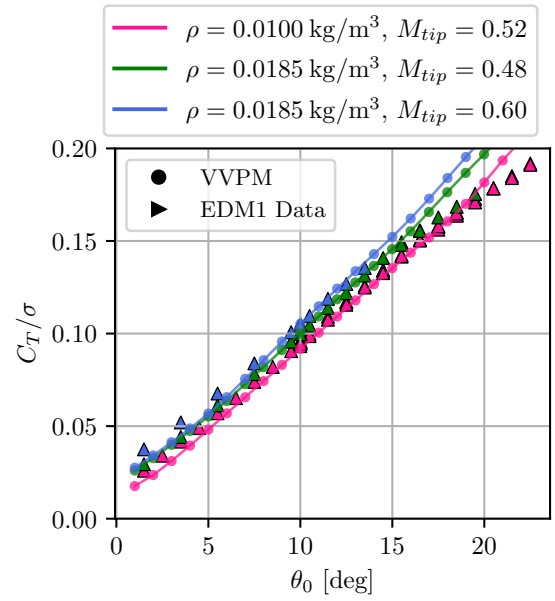

(a) Thrust vs. Collective.

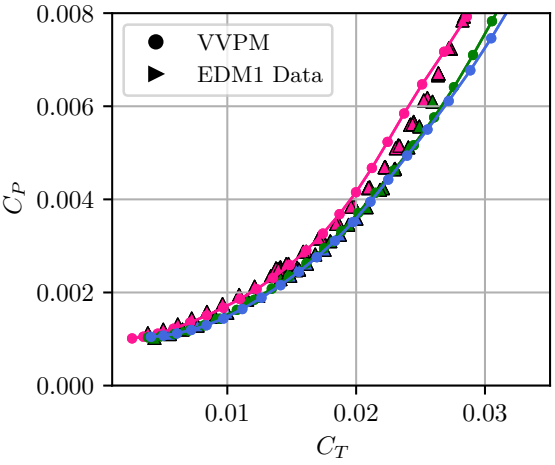

(b) Power vs. Thrust.

Figure 1. Comparison of experimental and VVPM predictions of thrust and power for EDM-1.

The numerical predictions of rotor thrust are shown to agree very well with the experimental data at the nominal operating blade loading $C_T/\sigma \approx 0.1$, and up to $C_T/\sigma \approx 0.15$. At the highest collectives, VVPM overpredicts the thrust. This holds particularly true for the higher density cases. A similar trend is seen in the power versus thrust predictions, where simulation and experiment show excellent correlation at low to mid thrust. While power is overpredicted for higher thrust at the lowest density, $\rho = 0.01$ kg/m^3, the opposite is true for $\rho = 0.0185$ kg/m^3. The predicted and measured Figure of Merit (FM) against blade loading C_T/σ is presented in Figure 2, once again showing a close comparison of rotor performance around the nominal operating point. In particular, the experimental peak Figure of Merit is predicted well across the range of considered test conditions.

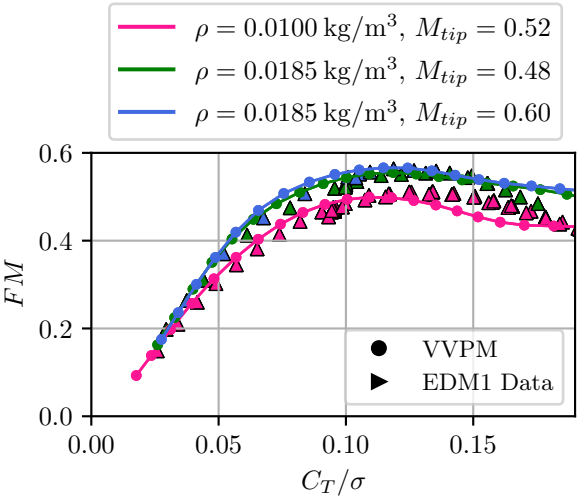

Figure 2. Comparison of experimental and VVPM simulation predictions of Figure of Merit.

Excellent matching of coaxial rotor performance is observed around the nominal operating blade loading of Ingenuity, but similar to Figure 1, VVPM predictions are seen to deviate from the experiments at increasingly higher blade loadings. At the higher density case, FM is over-predicted, while the opposite is true for the lower density. Modeling the (early) on-set and character of stall is a challenging task in general; the considered extreme flow regime adds yet another layer of complexity and is uncertain to date. The discrepancies in this region are partially attributed to shortcomings of the aerodynamic rotor model itself, but to what extent remains inconclusive in the current study. To contextualize the presented predictions, Koning (Ref. 8) previously analyzed the same dataset, comparing comprehensive CAMRADII simulations (lifting-line with free wake) against blade-resolved 3D CFD. Koning's findings indicated that while rotor performance metrics aligned reasonably well between computational approaches, discrepancies emerged when compared to experimental data, particularly at high blade loading. Additionally, slight deviations were observed in the computational versus measured slope in thrust versus collective angle. The magnitude and primary region of these discrepancies are comparable to those observed with VVPM for EDM-1. Notably, the present results exhibit more conservative performance predictions than both 2D and 3D CFD in Ref. 8, primarily due to modifications in the airfoil tables used in this study (Ref. 29). While the impact of wake dynamics modeling on coaxial rotor performance in hover is arguably less significant than in multi-rotor applications, the overall agreement with comparable—and higher-fidelity—simulations underscores VVPM's utility and substantiates its applicability in

the considered aerodynamic regime.

VVPM Predictions of Forward Flight Trim Compared to Flight Data

Compared to hover, the rotor wake in forward flight is convected downwards as well as aft of the rotor(s). An increasing advance ratio breaks the axis symmetry of rotor loads and induced wake due to the higher velocity of the advancing blade compared to the retreating side. The non-zero wake skew angle gives rise to a longitudinal inflow gradient, and the aerodynamic hub moments imparted by the emergent inflow gradients are counteracted by the cyclic control to achieve trim. Thus, the demanded cyclic control effort is a (steady-state, first-order) reflection of the rotor wake effects on the helicopter in forward flight. Owing to the low level of aerodynamic damping in the Mars atmosphere, the rotor system of Ingenuity was significantly stiffened to push the poorly damped flapping modes beyond the control system's bandwidth, reducing the risk of resonant coupling. The stiffening of the rotor effectively reduces the phase in the rotor tip-path plane (TPP) response to 1/rev excitation. Consequently, longitudinal control comes predominantly from the cosine cyclic (Ref. 9).

While a limited set of forward flight tests were conducted as part of the Verification & Validation (V&V) of Ingenuity, aspects of the wake modeling including interference effects as function of advance ratio remain unexplored. However, the end of Ingenuity's mission involved two system identification flights, namely Flight 68 and 69 (Ref. 30), with the objective of reducing modeling uncertainty in the forward flight regime. Trim data from the steady state segments of Flight 69 are used to correlate cyclic control effort against simulated VVPM trim solutions. Moreover, the control effort is contrasted against predictions using a three state dynamic inflow model as implemented in HeliCAT (Ref. 10), the primary flight dynamics and analysis tool used in the development of Ingenuity. In the dynamic inflow model, discrete inflow states are governed by a first-order system of equations based on the derivations presented in Ref. 11, with modifications to account for rotor-rotor interference and calibration based on experimental data. The lower rotor cyclic control effort is compared against trim data from Flight 69 in Figure 3. The estimated airspeed reaches approximately 15 m/s, exceeding both the forward flight speeds tested in the JPL SS and the aircraft's maximum authorized groundspeed of 10 m/s. While the lower airspeed segment is predicted sufficiently well with both models, the control asymptote with higher airspeed predicted with the dynamic inflow model seems to underpredict the actual control effort, where the VVPM predictions compare better with the flight data. Recall that a ramification of the stiff rotor system is an exacerbation of aerodynamic hub moments, and in consequence, a larger sensitivity to edgewise flow. This effect is hypothesized to be underpredicted with the dynamic inflow model (Ref. 31).

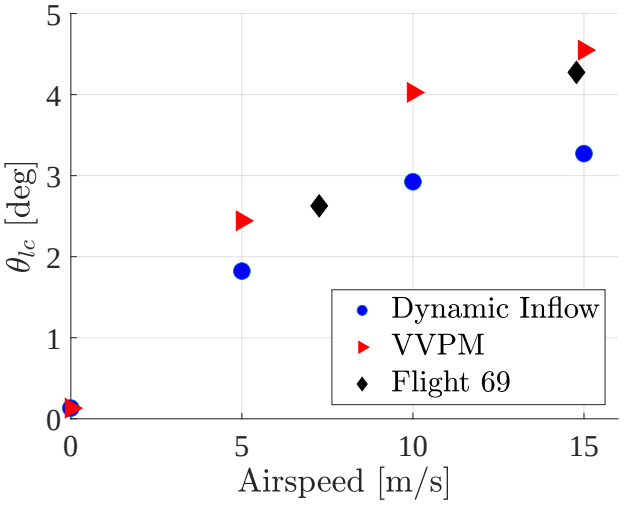

Figure 3. Comparison of cyclic control effort as function of airspeed, Flight 69.

Simulated Induced Rotor Wake and Coaxial Interference

Having presented the experimental results, the simulation data is studied in more detail in this section to provide further insight to the characteristics of the induced rotor wake. A high-level computational analysis, including rotor-rotor interference effects, of the Ingenuity rotor operating in hover and forward flight using VVPM is provided. The rotor reference frame is defined in Figure 4, with the x-axis positive in the downstream direction, opposite of the direction of forward flight. For ease of illustration, the same coordinate system will be referenced regardless of the rotational direction of the rotor, unless stated otherwise.

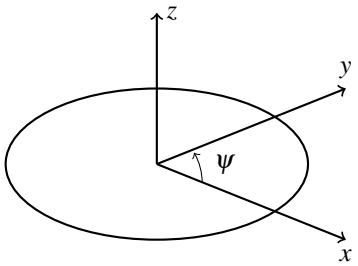

Figure 4. Rotor hub reference coordinates.

Hover The EDM-1 test campaign entailed a number of "trim runs" to find a collective setting for a target blade loading for subsequent runs. Two trim runs targeting blade loadings $C_T/\sigma = 0.135$ and $C_T/\sigma = 0.175$ at Case ID 1 conditions ($\rho = 0.01$ kg/m^3, $M_{tip} = 0.52$), are replicated in simulation with VVPM. The coaxial rotor system in simulation is trimmed to torque balance to assess the impact of interference on thrust share as predicted by VVPM. It is noted that this was not done in the experiments, nor was the test set-up equipped with individual rotor load measurement, prohibiting direct correlation of simulation with experimental data. The trim protocol as implemented in FLIGHTLAB and detailed

in Ref. 13 is inspired by loose coupling strategies with CFD, where the higher fidelity wake is active in the outer trim loop, and a reference, computationally cheap, inflow model is active in the inner trim loop. Let C_{T_u} and C_{T_l} denote the thrust coefficients of the upper and lower rotor, respectively. The resulting simulated thrust share and trim collective is tabulated in Table 4. At the lower blade loading $C_T/\sigma = 0.135$, closer to nominal operations of Ingenuity, the upper rotor provides 54 % of the total thrust, which is in agreement with the 53-56 % coaxial rotor thrust sharing reported for coaxial rotors on Earth in VVPM literature (Ref. 18). At the higher blade loading, the upper and lower rotor is seen to converge to an equal thrust share. The variation in thrust coefficient over one

Table 4. Simulated coaxial rotor thrust share in hover.

Trim C_T/σ	C_{T_u}/C_T	θ_u [deg]	θ_l [deg]
0.135	0.537	15.05	15.80
0.175	0.507	18.71	19.64

full revolution at these conditions are presented in Figure 5, where solid lines and dashed lines are for upper and lower rotor, respectively. In addition to illustrating the unequal thrust share, Figure 5 reveals the dominant 4/rev component due to bound circulation interaction at the blade passing of the two counter-rotating rotors. The impulsive change in thrust is slightly more prominent for the lower rotor, in particular for the higher thrust case.

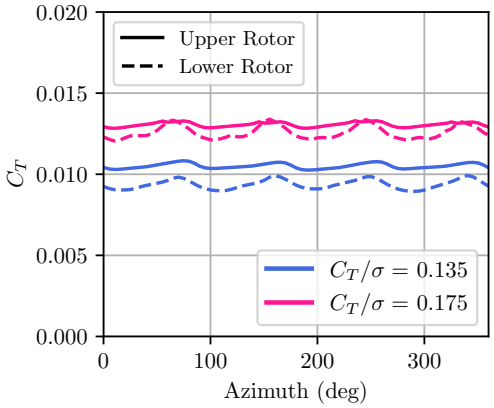

Figure 5. Trust variations in hover, trimmed to torque balance.

In addition to aggregate performance predictions, VVPM allows for direct analysis of the induced rotor wake structure, and a preliminary analysis of the hovering rotor wake of Ingenuity is presented. A vorticity magnitude (WM) contour in the $y-z$ plane passing through the hub center ($x = 0$) is shown in Figure 6, indicating the root and tip vortex positions and trajectories as the coaxial wake is convected below the rotor discs. The distinct vortices are retained to approximately $2R$ below the rotor hub, after which the coherent structure starts to break down and the wake dissipates.

While isolated rotor tip vortex trajectories in hover has shown to be accurately modeled with empirical formulations such as that of Langreber (Ref. 32), upper and lower tip vortex trajectories have been found to deviate for coaxial configurations in experiments (Ref. 33) and simulation, e.g. using a Vortex Transport Method (VTM) as shown in Ref. 34. The discrepancies are due to interference and vortex interaction effects in the near wake. A relatively smaller vertical rotor separation, such as the one of Ingenuity, increases the probability of inter-rotor vortex interaction.

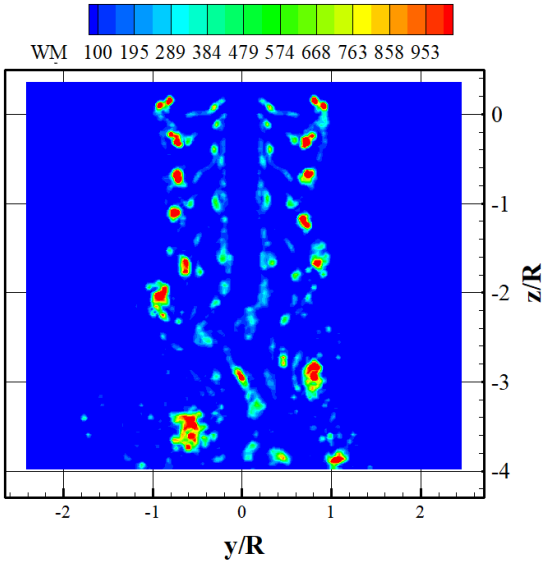

Figure 6. Vortex structure of Ingenuity's rotor wake in hover, expressed in vorticity magnitude WM, sliced at x = 0. ρ = 0.01 kg/m^3, M_{tip}= 0.52, C_T/σ= 0.135.

A closer field of view is presented Figure 7, where the upper rotor tip vortices are seen to travel radially inward as the upper rotor wake contracts into an inner "tube".

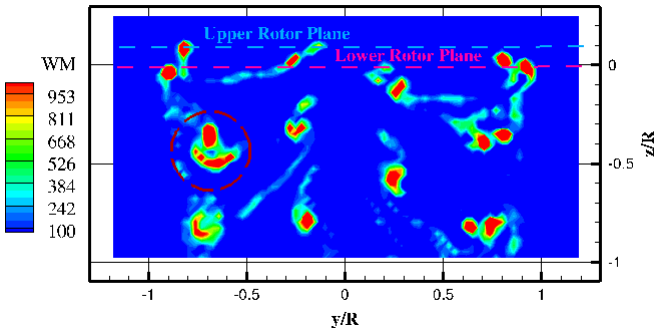

Figure 7. Near-wake vortex interactions in hover at x = 0, expressed in vorticity magnitude WM. ρ = 0.01 kg/m^3, M_{tip}= 0.52, C_T/σ= 0.135.

The vortex pairing, circulated in red, indicates an inter-rotor vortex interaction. No characterization of the rotor induced flow field was done as part of the test campaigns of Ingenuity, prohibiting experimental comparisons of these effects. A comprehensive study of tip vortex trajectories, interactions,

and (sheet) geometry, and their dependency on Reynolds number, is out of the scope of this paper and will be considered in future work.

To characterize the rotor induced velocity distributions, a set of stationary sampling points distributed radially (14 stations) and azimuthally (every 10 degrees) probe the velocity field at the upper and lower rotor disk planes. Time averages of non-dimensionalized, radial induced velocity distributions, $\lambda_i = v_i/(R\Omega)$, defined positive for a net velocity downwards are presented in Figure 8, sliced at $y = 0$.

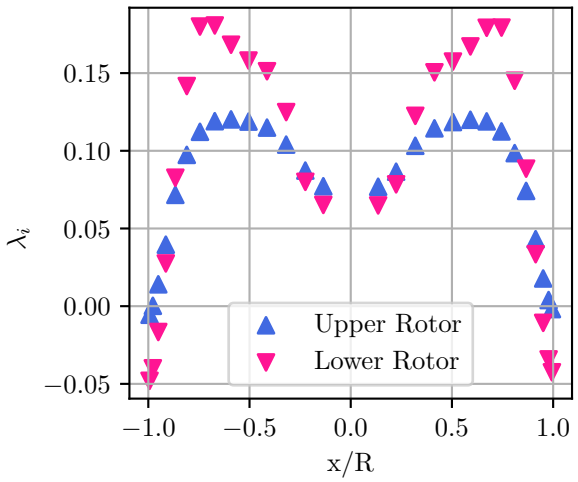

Figure 8. Induced velocity distributions, sliced at y = 0. C_T/σ = 0.135.

For the coaxial configuration, non-uniform rotor-rotor interference is dominantly coming from the upper to the lower rotor. Even though the lower rotor operates at slightly lower thrust to achieve torque balance, the induced velocity inboard of $r/R \leq 0.9$ is significantly larger due to the interference. The radial variation is more dramatic, showing a sharp gradient and peak around where the mean trajectory of the tip vortices of the upper rotor impacts the lower. Contraction of the upper wake before it reaches the lower rotor exaggerates the tip upwash on the lower rotor.

Forward Flight This section presents a qualitative and quantitative characterization of the forward flight rotor wake of Ingenuity. Snapshots of the rotor wake in Figure 9 as predicted for Ingenuity at airspeed 15 m/s, $\mu = 0.1$, illustrates the development of the wake downstream. The sliced iso-surface in the x-z plane passing through the rotor hub in Figure 9a shows how, in addition to the individual interaction with its own wake, the trailed tip vortices from the upper rotor all pass through the lower rotor plane. The top-down view in Figure 9b shows the complex vortex roll-up of coaxial rotors, with interlocking of both the upper and lower rotor trailed tip vortices to form characteristic supervortices. The corresponding effect on the induced velocities over the rotor disks (averaged over 10 revolutions) are presented in the polar distributions in Figure 10. The inter-rotor blade-vortex interactions (BVIs) result in a non-uniform distortion of the lower rotor inflow distribution. In contrast to the axisymmetric distribution seen in Figure 8, inflow gradients are seen to form in forward flight over the rotors in radial the inflow distributions shown in Figure 11.

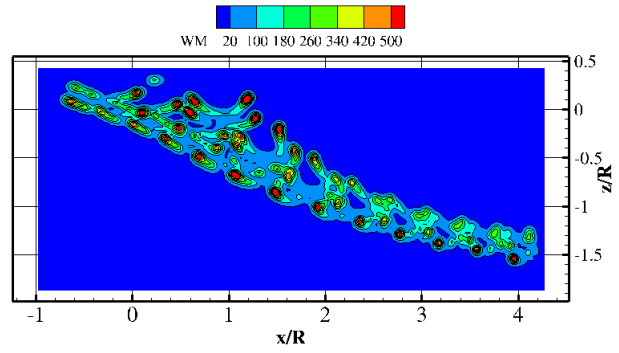

(a) Wake structure sliced at y = 0.

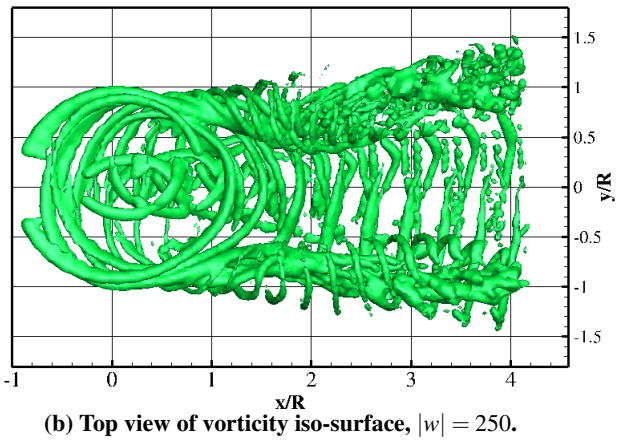

(b) Top view of vorticity iso-surface, $|w| = 250$.

Figure 9. Wake structure in forward flight, μ= 0.1.

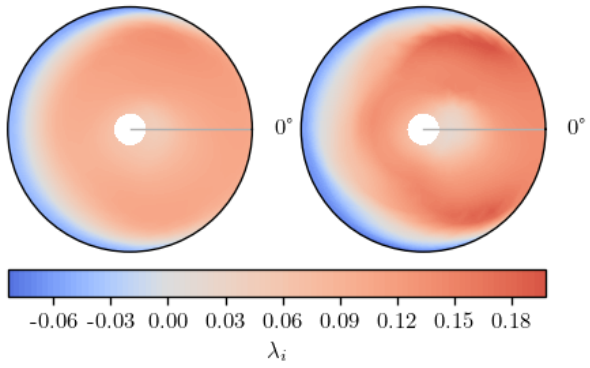

Figure 10. Induced velocity distributions in forward flight, μ= 0.1. Left: Upper (CCW). Right: Lower (CW).

An orderly longitudinal gradient is observed at the slice $y = 0$ in Figure 11a. As in hover, sharper gradients are observed in the distribution for the lower rotor, owing to interactions with the upper rotor wake. The lateral distribution in Figure 11b shows the relative increase in induced velocity on the advancing side ($y > 0$) of the upper rotor, as would be observed for an

isolated rotor. For the coaxial rotor, the increase in strength of advancing side tip vortex results in a sharp impulse-like perturbation as it hits the lower rotor.

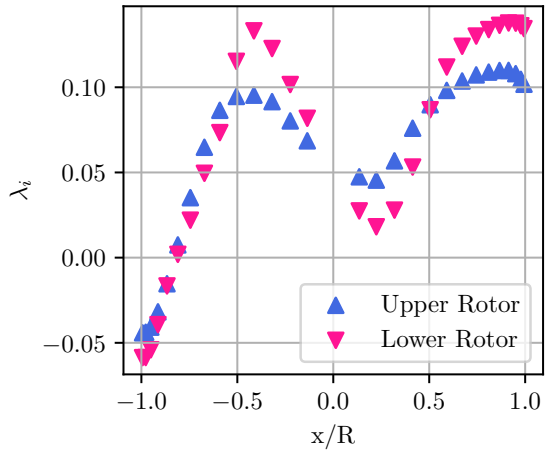

(a) Sliced at y = 0.

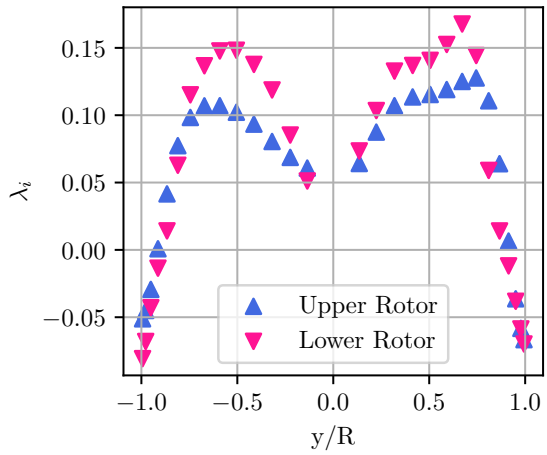

(b) Sliced at x = 0.

Figure 11. Induced velocity distributions in forward flight, $\mu = 0.1$.

NEXT GENERATION MARS ROTORCRAFT

Following the success of the Ingenuity Mars Helicopter, more capable vehicles are being proposed for the next generation of Mars rotorcraft. In particular, larger scale multi-rotor configurations with a significant increase in liftoff mass are being considered, e.g., to allow for higher scientific payload. In addition, expanding the forward flight envelope beyond the small advance ratios of Ingenuity will also allow for longer range missions. The conceptual design of the Mars Science Helicopter (Ref. 1) served as a reference vehicle for the sizing study by Grip in Ref. 4, resulting in the baseline design of the hexacopter referred to in the following as Chopper, shown in a CAD rendering in Figure 12. The sheer increase in the number of rotors operating in close proximity, combined with higher advance ratios, underscores the need for careful modeling of the rotor wakes across the full flight envelope. Accurately modeling the aerodynamic performance is critical to inform optimal control allocation and a fair assessment of stability and control authority margins. This section gives a preliminary characterization of the dominating rotor-interference effects seen with Chopper, as predicted by VVPM.

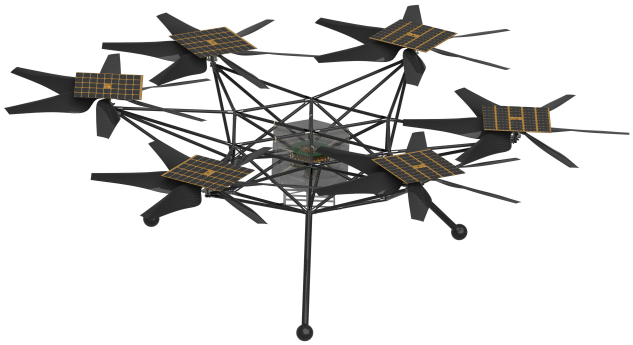

Figure 12. Rendering of Chopper, conceptual design. Credit: NASA JPL (Ref. 4). Rotor Credit: NASA Ames (Ref. 35).

A schematic of the baselined Chopper configuration rotor indexing and direction of rotation is presented in Figure 13 (not to scale). While the rotor radius $R = 0.675$ m falls in between Ingenuity and SRH, the Chopper rotors have a much increased solidity, $\sigma = 0.3$, to support the large-scale vehicle while minimizing footprint. Rotors with odd indices (1,3,5) are placed approximately $0.15R$ above rotors with even indices (2,4,6), and are illustrated with solid and dashed lines, respectively. As illustrated in Figure 13, the rotor disks have a non-zero overlap of $0.11R$, retaining compactness to comply with the geometric constraints of the reference aeroshell. For the benefit of the reader, rotors at the same longitudinal coordinate are paired in colors, with front (1, 6), mid (2, 5), and aft (3, 4) in green, orange and red, respectively. Unless stated otherwise, all simulated results in this section are at a fixed atmospheric density $\rho = 0.0121$ kg/m^3 and tip Mach number $M_{tip} = 0.748$.

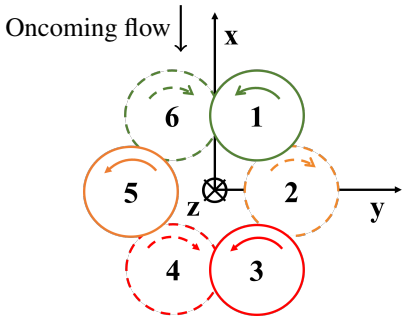

Figure 13. Planform view schematic of Chopper rotor layout configuration.

Wake Effects on Aerodynamic Loads

A VVPM prediction of the wake geometry for Chopper in trimmed forward flight at a longitudinal airspeed of 30 m/s

($\mu = 0.165$) is shown in Figure 14, providing an appreciation for the complexity of the flow field and the intra- and inter-rotor wake interactions at play. Oncoming flow from

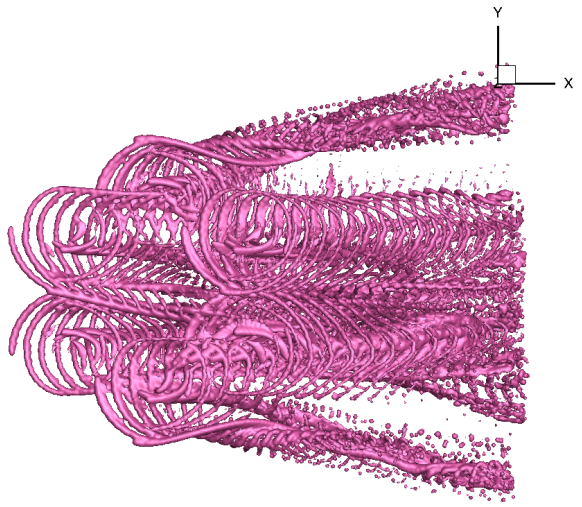

Figure 14. Wake structure of Chopper in forward flight, $\mu = 0.15$.

interfering rotors will impact the effective angle of attack of the blades, and in direct consequence, the control effort required for a given thrust and trimmed flight condition. As a first order assessment of interference effects on control margin, Figure 15 shows the trim collective control effort for a longitudinal airspeed up to 50 m/s.

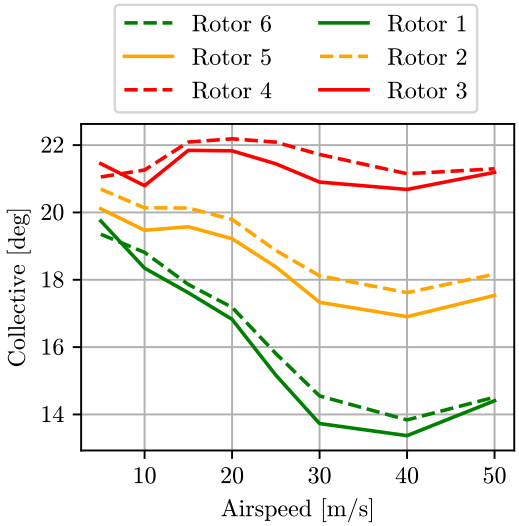

Figure 15. Collective trim solutions.

Due to the inclusion of rotor-rotor interference, differentials between rotor trim collectives are observed in the two horizontal planes (dashed versus solid lines), an effect that an interference agnostic model would fail to predict.

The azimuthally varying rotor loading due to the interaction of the wake and rotor blades is studied next. The influence of the VVPM wake on the unsteady rotor vertical forces over one revolution is presented for a low- and high speed case in Figure 16a and Figure 16b, respectively. At low speed ($\mu = 0.0275$), the thrust share across rotors is evenly distributed, yet a strong N_b/rev component is observed on the rotors in the lower horizontal plane due to blade-vortex interactions in the rotor disk overlaps. At the (relative) high-speed forward flight, $\mu = 0.275$, the thrust share is weighted towards the aft rotors (red) to pitch the thrust vector and counteract the drag induced pitch moment.

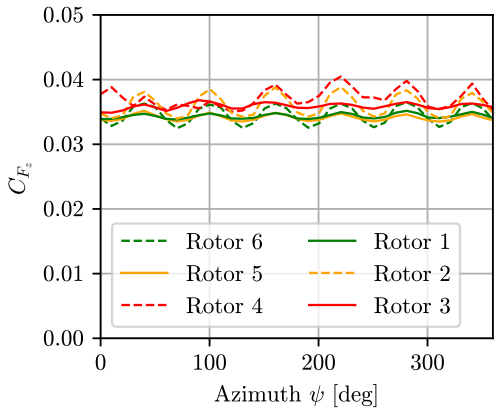

(a) $\mu = 0.0275$.

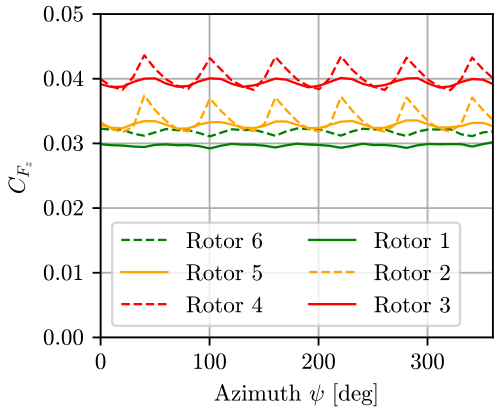

(b) $\mu = 0.275$.

Figure 16. Rotor vertical force variations over one revolution.

The mid and aft rotors in the lower horizontal plane (2,4) experience a sharp N_b/rev loading due to the wake of the upstream rotors. However, this effect is mitigated and phase-shifted for the front rotor (Rotor 6), which is primarily influenced by the interaction with the retreating tip vortex of the side-by-side rotor (Rotor 1). The dimensionless induced velocity distributions over the disks reveal the origins of these loads with greater detail and are presented in Figure 17, again contrasting a near-hover case (Figure 17a) with high-speed forward flight (Figure 17b). The upper rotor vortices hitting the lower rotors at the rotor disk overlap gives a significant

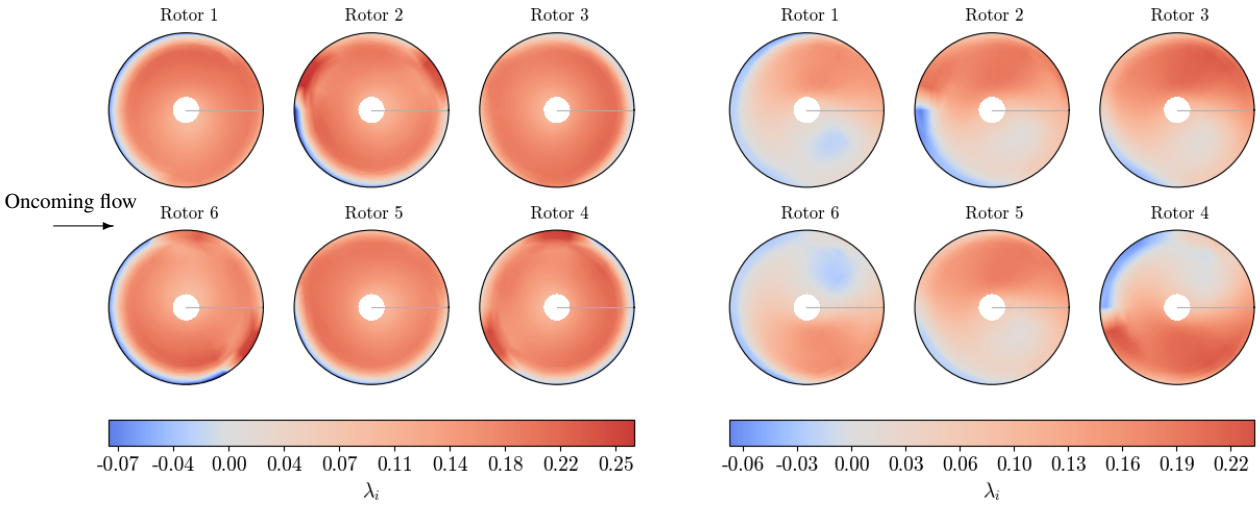

(a) μ = 0.0275. **(b) μ = 0.275.**

Figure 17. Comparison of induced velocity distributions in low and high-speed forward flight.

non-uniform distortion of the inflow distribution, even near hover. In high-speed forward flight, the difference in speed of advancing and retreating blades gives rise to a distinct lateral inflow gradient. This effect is super-imposed with the interference from upstream to downstream rotors, where alternating rotational directions align the advancing sides within the same y-coordinate corridor. In contrast, pairs (1,6) and (3,4) enjoy a mutual upwash effect as orderly observed for rotors in side-by-side configurations, that in fact has a net-positive effect on rotor efficiency.

To single out the effects attributable to rotor-rotor interference, the sampled induced velocity distribution over the rotor disks when including interference from the VVPM wake, as illustrated in Figure 17, is compared against self-induced velocities from an isolated rotor trimmed to the equivalent thrust and flight condition.

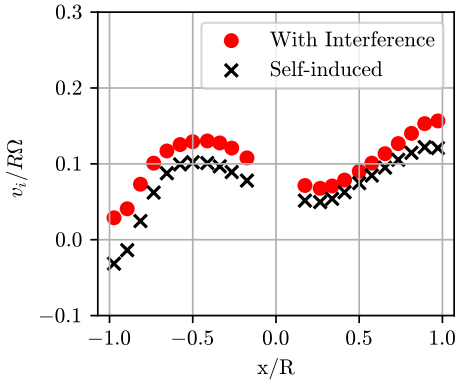

Figure 18. Radial inflow distribution of Rotor 3 at y = 0, μ = 0.275.

The aftmost rotors in forward flight pose a particularly interesting case for interference and are studied more closely. They are expected to encounter portions of both the front and mid rotor wake as the vehicle translates forward, as well as a mutual, pairwise side-by-side interference effect. The time-averaged longitudinal inflow distribution for Rotor 3, the aftmost rotor in the upper horizontal plane, is shown in Figure 18. In addition to a uniform downwash, which yields a positive bias to the distribution, an increased velocity at the front of the rotor disk arises due to interference from upstream rotors, similar to the effect observed in Ref. 36.

Next, the sharp variation in rotor loads due to the disk overlap is highlighted for Rotor 4, the aftmost rotor in the lower horizontal plane. Figure 19 shows the azimuthally varying induced velocity at $r/R = 0.75$. Note that while the Rotor 4 spins clockwise, the azimuthal angle ψ is defined positive counterclockwise for visualization.

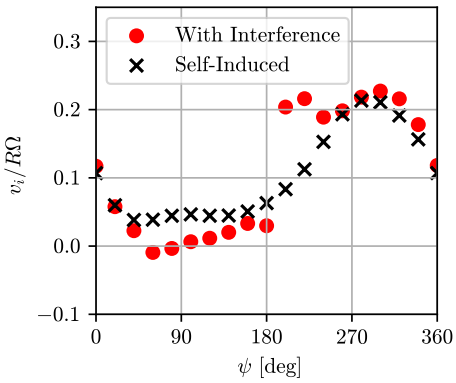

Figure 19. Azimuthal inflow distribution of Rotor 4 at r/R= 0.75, μ = 0.275.

Where the isolated rotor shows a smooth transition from advancing to retreating side in the induced velocity distribution, the tip vortex from the rotor in the plane above yields a close-to discontinuous jump for Rotor 4 around $\psi = 190$ deg when including interference.

REDUCED-ORDER ROTOR-ROTOR INTERFERENCE

The previous section highlights that rotor-to-rotor interference significantly impacts aerodynamic performance and unsteady aerodynamic loads on the rotors in non-trivial ways. Inevitably, these effects propagate to structural dynamics as well as flight dynamics. Modeling rotor-rotor interference effects becomes imperative for a successful control design. The computational efficiency and parallel nature of VVPM, makes analyzing a wide range of cases off-line feasible. However, it is still not applicable to real-time simulation, and is not readily linearizable. This section outlines an approach similar to that developed and validated for Advanced Air Mobility (AAM) applications in Ref. 21, to emulate the higher-fidelity VVPM data with a reduced order model that is compatible with finite-state dynamic inflow models commonly employed for flight dynamics predictions.

Model Formulation

An additive interference effect is formulated in Equation (3), assuming that interference contributions are independent and can be superimposed to the self-induced wake,

$$w_i(r_i,\psi_i,t) = w_i^{ind}(r_i,\psi_i,t) + w_i^{intf}(r_i,\psi_i,t), \tag{3}$$

where r_i and ψ_i are the radial and azimuthal locations on the i:th rotor disk. A state-space representation to compute w_i^{intf}, as in Ref. 21, is considered. With a three-state interference model, the conventional harmonic expansion consists of a uniform component, $w_0^{intf}(r_i,\psi_t,t) \cong w_0(t)$, and a linear variation over the disk, $\propto r_i(w_c^{intf}(t)\cos(\psi_i) + w_s^{intf}(t)\sin(\psi_i))$. The interference states are related to the aerodynamnic load coefficients of the interfering rotors through a variable block matrix denoted by M as defined in Equation (4), parameterized with the advance ratios $M := M(\boldsymbol{\mu})$. For a hexacopter, this matrix is a 18×18 square block matrix. As such, every matrix $M_{ij} \in \mathbb{R}^{3\times 3}$ contains coefficients that relate the aerodynamic loads of rotor j to its interference contributions onto rotor i.

$$\mathbf{M}(\boldsymbol{\mu}) = \begin{bmatrix} 0 & M_{12} & \dots \\ \vdots & \ddots & \vdots \\ M_{N_R 1} & \dots & 0 \end{bmatrix}, \quad \text{where} \tag{4}$$

$$\mathbf{M} \in \mathbb{R}^{3N_R \times 3N_R}, \quad M_{ij} \in \mathbb{R}^{3\times 3} \tag{5}$$

At a given time and flight condition, the total interference contributions to rotor i are computed through Equation (6). The gain matrix coefficients are multiplied by the aerodynamic load coefficients of the rotor that is imparting interference, in a similar vein as for a finite-state dynamic inflow model. This now allows to query the model to obtain the interference state vector $\mathbf{w}^{intf}$ at any flight conditions within the bounds of the generated data.

$$\frac{\boldsymbol{w}_i^{intf}}{R\Omega} = \boldsymbol{\lambda}_i^{intf} = \begin{bmatrix} \lambda_{i,0}^{intf} \\ \lambda_{i,c}^{intf} \\ \lambda_{i,s}^{intf} \end{bmatrix}_j = \sum_j M_{ij}(\boldsymbol{\mu}) \begin{bmatrix} C_T \\ C_L \\ C_M \end{bmatrix}_j \tag{6}$$

Data Generation

The formulation in Equation (6) is predicated upon extraction of individual rotor contributions to the aggregate, experienced interference velocity distribution for every rotor. A heuristic methodology to do so was developed and is summarized in Figure 21. From the left, full vehicle trim runs provide steady state data, specifically the trimmed thrust and lateral/longitudinal moments, C_T, C_L and C_M, respectively. Collecting the time averaged aerodynamic coefficients and advance ratios from the trim solutions, identical isolated rotors are trimmed to equivalent thrust to back out the self-induced velocity distribution the rotor would experience would no other rotor wake impart interference. Analogously, every pair of rotors is also trimmed to the equivalent thrust from the full configuration to obtain the pairwise interference velocity distribution λ_{ij}. An example wake structure from a pair-wise run (Rotor 5 and 6) is provided for illustration in Figure 20.

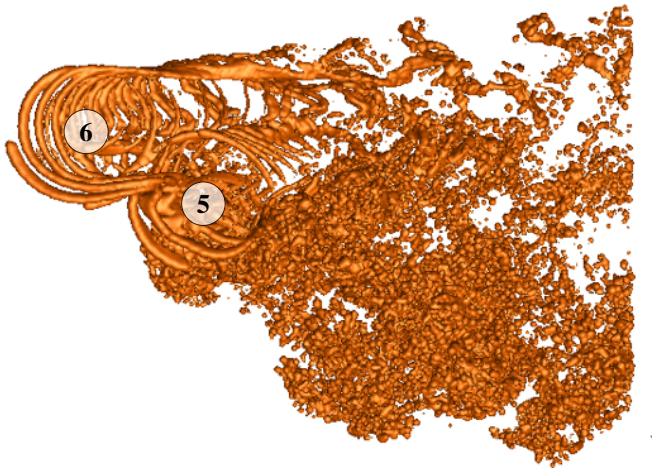

Figure 20. Pairwise rotor wake structure for rotor pair (5, 6) in forward flight.

To derive the interference matrix coefficients, the pairwise distributions are normalized with the interfering rotor's trimmed aerodynamic load coefficients $[C_T, C_L, C_M]_j^T$. It is noted that a limitation of the formulation Equation (6) and Figure 21 is that any nonlinear dependencies or cross-correlations between rotors are ignored. Using this method, the data generation for a single interference matrix requires one full vehicle trim case, N_r isolated trim cases and $\binom{N_r}{2}$ pairwise trim runs. For a given configuration, however, symmetries can be exploited to reduce the number of runs for a set of flight conditions.

Example Results

Following the approach outlined in Figure 21, a model is derived for the Chopper vehicle across the full flight envelope with a total of more than 160 flight conditions, including high-speed forward flight as well as lateral and vertical winds. For this demonstration, only a uniform interference component as function of rotor thrust is considered, which reduces the size

of the interference gain matrix to a 6×6 matrix. An illustration of the collected normalized pair-wise uniform interference components, $\lambda_{0,ij}^{intf}$, for three distinct flight conditions is presented in Figure 22. Each square in the matrix represents a rotor pair, where a row index i corresponds to rotor i receiving interference from the rotor j indexed by the column j. A red square indicates downwash, meaning an oncoming flow from above as experienced by the receiving rotor, and a blue square denotes a net upward velocity, or upwash. As anticipated, a dominating downwash on aft rotors caused by rotors in front in the same y-coordinate corridor is observed. Mutual upwash is predicted for side-by-side rotor pairs, which agrees with what is commonly seen for side-by-side rotors, and acts to mitigate the adverse downwash. This result emphasizes the complexity of interference patterns in an advanced multirotor configuration, where competing interference effects combine into net influences that are challenging to predict in advance. As seen from the asymmetry across the diagonal of Figure 22, the biplane positioning of the rotors break the axisymmetry, as was also indicated by the trimmed control effort in Figure 15.

To arrive at a continuous model, the interference gain matrices are interpolated as a function of advance ratio. To evaluate the soundness of the interpolation approach, Figure 23 presents an interference gain matrix at a a validation scenario: a longitudinal velocity of 35 m/s ($\mu_x \approx 0.19$) and horizontal flight path angle $\gamma_h = 10$, a flight condition that was not explicitly included in the simulation database. Linear interpolation based on advance ratio was used to arrive at the middle matrix in Figure 22b. To the right-most in Figure 22c, the interpolation error is quantified by taking the absolute difference between the true and interpolated interference matrices for the given flight condition. The errors are sufficiently small, confirming that a linear interpolation protocol provides adequate accuracy without requiring finer discretization in the dataset parameterization, around this particular flight condition. With the interference gain matrices established, first-order interference effects can now be incorporated into relevant flight dynamics models by augmenting the induced inflow output equation with Equation (3).

CONCLUSIONS

The applicability of a Viscous Vortex Particle Method for rotor wake analysis of previous and next-generation of Mars rotorcraft was established. Predicted and measured coaxial rotor performance metrics showed excellent agreement around the nominal operating blade loading and peak Figure of Merit, with discrepancies observed at the highest blade loadings. Predictions of cyclic control efforts at high-speed forward flight with the VVPM wake was seen to agree well with Ingenuity flight data. The simulated coaxial rotor wake was analyzed, showing the dominant impact of wake interference on the performance and unsteady loading of the lower rotor, contrasting hover and forward flight wake interaction characteristics. Having indicated applicability of the VVPM wake model in the low Reynolds number high-subsonic aerodynamic regime, a next generation large-scale Mars hexacopter was analyzed using VVPM. Complex rotor wake dynamics, including blade-vortex-interactions, pair-wise tandem interference and downwash from vertically separated rotors were well captured by the wake model. Finally, a method to derive state-space representations of first-order interference effects was presented and applied to the Mars hexacopter. Simulation data was generated across a wide range of flight conditions, showcasing the applicability of VVPM as a computationally tractable mid-fidelity tool for Mars rotorcraft wake predictions and reduced-order modelling of rotor-rotor interference. Author contact:

- Tove Ågren tove.s.aagren@nasa.gov
- Allen Ruan allen.w.ruan@nasa.gov

FUTURE WORK

This work did not exhaustively cover rotor wake effects of particular interest at low Reynolds numbers. Phenomena related to viscous wake effects are likely to be more prominent at these conditions: work by Shukla (Ref. 12) has shown unexpected viscous effects in an experiment related to swirl recovery in coaxial-like configurations at Reynolds numbers down to 40k, which is still significantly larger than studied herein. Replicating these effects in the current simulation framework would provide further indication of the utility of VVPM for Mars rotorcraft application. The rotor-rotor interference model for Chopper is currently being coupled with a dynamic inflow model to assess the implications on flight dynamics. Model improvements are underway, including interference gradients, time delays to capture first-order wake dynamic effects, and interpolation protocols to better emulate non-linear interference effects with advance ratio.

ACKNOWLEDGMENTS

This work was carried out under funding from the New Business Council at NASA Ames Research Center, which the authors thank for their resources and support. The authors would like to thank Wayne Johnson, Carlos Malpica and Natasha Schatzman for their technical advice and mentoring, and Witold Koning, Jason Cornelius and Sesi Kottapalli for their editorial feedback. Acknowledgements are extended to the Ingenuity and Chopper teams at the NASA Jet Propulsion Laboraory. The authors would also like to thank ART for technical support on FLIGHTLAB VVPM implementations. Finally, the authors would like to acknowledge the support of William Warmbrodt and Larry Hogle during this research.

REFERENCES

1. Johnson, W., Withrow-Maser, S., Young, L., Malpica, C., Koning, W. J. F., Kuang, W., Fehler, M., Tuano, A., Chan, A., Datta, A., Chi, C., Lumba, R., Escobar, D., Balaram, J., Tzanetos, T., and Grip, H., "Mars Science Helicopter Conceptual Design," NASA TM 220485, 2020.

2. Tzanetos, T., Bapst, J., Kubiak, G., Tosi, L. P., Sirlin, S., Brockers, R., Delaune, J., Grip, H. F., Matthies, L., Balaram, J. B., Withrow-Maser, S., Johnson, W., Young, L., and Pipenberg, B., "Future of Mars rotorcraft-Mars science helicopter," 2022 IEEE Aerospace Conference (AERO), Big Sky, MT, USA, March 2022. DOI: 10.1109/AERO53065.2022.9843501.

3. Withrow-Maser, S., Johnson, W., Koning, W. J., Aagren, T., Sahragard-Monfared, G., Bowman, J., Ruan, A., Kaweesa, D., and Malpica, C., "Critical Aerodynamic and Performance Upgrades to Enable Larger Mars Rotorcraft Such as the Chopper Platform," Vertical Flight Society 81st Annual Forum & Technology Display, Virginia Beach, VA, USA, May 2025.

4. Grip, H. F., Jones-Wilson, L., Lefler, C., Duran, A., Inouye, B., Burns, B., Metz, B., Brown, T., Bugby, D., Karras, J., Mier-Hicks, F., Tzanetos, T., Johnson, W., and Ueno, M., "The CHOPPER Next-Generation Mars Rotorcraft: Scaling Ingenuity by a Factor 20," IEEE, Big Sky, MT, USA, February 2025.

5. Ruan, A., and Aagren, T., "Flight Dynamics Prediction for Scaled Mars Rotorcraft," Vertical Flight Society 81st Annual Forum & Technology Display, Virginia Beach, VA, USA, May 2025.

6. Grip, H. F., Johnson, W., Malpica, C., Scharf, D. P., Mandic, M., Young, L., Allan, B., Mettler, B., and San Martin, M., "Flight Dynamics of a Mars Helicopter," 43rd European Rotorcraft Forum, Milan, Italy, September 2017.

7. Koning, W. J., Johnson, W., and Grip, H. F., "Improved Mars Helicopter Aerodynamic Rotor Model for Comprehensive Analyses," *AIAA Journal*, Vol. 57, (9), 2019, pp. 3969–3979. DOI: 10.2514/1.J058045.

8. Koning, W. J., Allen, B., Romander, E., and Johnson, W., "Comparing 3D and 2D CFD for Mars Helicopter Ingenuity Rotor Performance Prediction," 49th European Rotorcraft Forum, Bückeburg, Germany, September 2023.

9. Grip, H. F., Johnson, W., Malpica, C., Scharf, D. P., Mandić, M., Young, L., Allan, B., Mettler, B., Martin, M. S., and Lam, J., "Modeling and Identification of Hover Flight Dynamics for NASA's Mars Helicopter," *Journal of Guidance, Control, and Dynamics*, Vol. 43, (2), 2020, pp. 179–194. DOI: 10.2514/1.G004228.

10. Leake, C., Grip, H., Steyert, V., Hasseler, T. D., Cacan, M., and Jain, A., "HeliCAT-DARTS: A High Fidelity, Closed-Loop Rotorcraft Simulator for Planetary Exploration," *Aerospace*, Vol. 11, (9), 2024, pp. 727. DOI: 10.3390/aerospace11090727.

11. Peters, D. A., and HaQuang, N., "Dynamic Inflow for Practical Applications," *Journal of the American Helicopter Society*, Vol. 33, 1988, pp. 64–68.

12. Shukla, D., and Komerath, N., "Low Reynolds number multirotor aerodynamic wake interactions," *Experiments in Fluids*, Vol. 60, 2019, pp. 1–14. DOI: 10.1007/s00348-019-2724-3.

13. Zhao, J., and He, C., "A Viscous Vortex Particle Model for Rotor Wake and Interference analysis," *Journal of the American Helicopter Society*, Vol. 55, (1), 2010, pp. 12007–12007. DOI: 10.4050/JAHS.55.012007.

14. He, C., and Rajmohan, N., "Modeling the Aerodynamic Interaction of Multiple Rotor Vehicles and Compound Rotorcraft with Viscous Vortex Particle Method," American Helicopter Society's 72nd Annual Forum, Vol. 18, West Palm Beach, FL, USA, May 2016.

15. Tan, J.-f., and Wang, H.-w., "Simulating Unsteady Aerodynamics of Helicopter Rotor with Panel/Viscous Vortex Particle Method," *Aerospace Science and Technology*, Vol. 30, (1), 2013, pp. 255–268. DOI: 10.1016/j.ast.2013.08.010.

16. He, C., Syal, M., Tischler, M. B., and Juhasz, O., "State-space Inflow Model Identification from Viscous Vortex Particle Method for Advanced Rotorcraft Configurations," American Helicopter Society's 73rd Annual Forum, Fort Worth, TX, USA, May 2017. DOI: 10.4050/F-0073-2017-12103.

17. Alvarez, E. J., and Ning, A., "High-fidelity Modeling of Multirotor Aerodynamic Interactions for Aircraft Design," *AIAA Journal*, Vol. 58, (10), 2020, pp. 4385–4400. DOI: 10.2514/1.J059178.

18. Singh, P., and Friedmann, P. P., "A computational Fluid Dynamics-based Viscous Vortex Particle Method for Coaxial Rotor Interaction Calculations in Hover," *Journal of the American Helicopter Society*, Vol. 63, (4), October 2018, pp. 1–13. DOI: 10.4050/JAHS.63.042002.

19. Friderichsen, J. H., "Rotor Wake Analysis Using the Viscous Vortex Particle Method," Master's thesis, KTH Royal Institute of Technology, 2024.

20. Zhao, J., and He, C., "A Finite State Dynamic Wake Model Enhanced with Vortex Particle Method–Derived Modeling Parameters for Coaxial Rotor Simulation and Analysis," *Journal of the American Helicopter Society*, Vol. 61, (2), April 2016, pp. 1–9. DOI: 10.4050/JAHS.61.022011.

21. Gladfelter, M., He, C., Chang, C., Tischler, M. B., Lopez, M. J., and Juhasz, O., "Enhancement and Validation of VPM-Derived State-Space Inflow Models for Multi-Rotor Simulation," Vertical Flight Society's 76th Annual Forum, Virginia Beach, VA, USA, October 2020. DOI: 10.4050/F-0076-2020-16287.

22. Guner, F., Prasad, J., He, C., and Peters, D., "Fidelity Enhancement of a Multirotor Dynamic Inflow Model via System Identification," *Journal of the American Helicopter Society*, Vol. 67, (2), April 2022, pp. 1–17. DOI: 10.4050/F-0077-2021-16832.

23. Du Val, R., and He, C., "Validation of the FLIGHTLAB Virtual Engineering Toolset," *The Aeronautical Journal*, Vol. 122, (1250), 2018, pp. 519–555. DOI: 10.1017/aer.2018.12.

24. He, C., and Zhao, J., "Modeling Rotor Wake dynamics with Viscous Vortex Particle Method," *AIAA Journal*, Vol. 47, (4), 2009, pp. 902–915. DOI: 10.2514/1.36466.

25. Ploumhans, P., Winckelmans, G. S., Salmon, J. K., Leonard, A., and Warren, M. S., "Vortex Methods for Direct Numerical Simulation of Three-dimensional Bluff Body Flows: Application to the Sphere at Re= 300, 500, and 1000," *Journal of Computational Physics*, Vol. 178, (2), 2002, pp. 427–463. DOI: 10.1006/jcph.2002.7035.

26. Withrow-Maser, S., Johnson, W., Tzanetos, T., Grip, H., Koning, W., Schatzman, N., Young, L., Chan, A., Ruan, A., Cummings, H., Brian, A., Malpica, C., Meyn, L., Pipenberg, B., and Keennon, M., "Mars Sample Recovery Helicopter: Rotorcraft to Retrieve the First Samples from the Martian Surface," Vertical Flight Society's 79th Annual Forum & Technology Display, West Palm Beach, FL, USA, May 2023. DOI: 10.4050/F-0079-2023-17969.

27. Schatzman, N., Chan, A., Gehlot, V., and Glazebrook, K. J., "Data Processing and Analysis of Performance Measurements from Ingenuity Rotors in the Jet Propulsion Laboratory 25-ft Space Simulator," Vertical Flights Society's 6th Decennial Aeromechanics Specialists' Conference, Santa Clara, CA, USA, February 2024. DOI: 10.4050/F-0080-2024-1357.

28. Schatzman, N., Chan, A., Fillman, M., Meyn, L., Gehlot, V., Glazebrook, K., Santillan, D., and Ridland, P., "Performance Analysis and Data Processing for the Mars Sample Recovery Helicopter in the Jet Propulsion Laboratory 25-ft Space Simulator," Vertical Flight Society's 80th Annual Forum & Technology Display, Montréal, Canada, May 2024.

29. Bowman, J., Dominguez, M., Johnson, W., Koning, W. J., Sahragard-Monfared, G., Schatzman, N., and Wright, S., "Airfoil Table Modification for Improved Calculation of Ingenuity Rotor Performance," NASA TM 0002920, 2024.

30. Aagren, T. S., Ruan, A. W., Malpica, C., Withrow-Maser, S., and Meyn, L., "In-flight System Identification of the Ingenuity Mars Helicopter," AIAA SciTech 2025 Forum, Orlando, FL, USA, January 2025. DOI: 10.2514/6.2025-0007.

31. Grip, H. F., Conway, D., Lam, J., Williams, N., Golombek, M. P., Brockers, R., Mischna, M., and Cacan, M. R., "Flying a Helicopter on Mars: How Ingenuity's Flights were Planned, Executed, and Analyzed," 2022 IEEE Aerospace Conference (AERO), Big Sky, MT, USA, March 2022. DOI: 10.1109/AERO53065.2022.9843813.

32. Landgrebe, A. J., "The Wake Geometry of a Hovering Helicopter Rotor and its Influence on Rotor Performance," *Journal of the American Helicopter Society*, Vol. 17, (4), 1972, pp. 3–15. DOI: 10.4050/JAHS.17.4.3.

33. Silwal, L., and Raghav, V., "Preliminary Study of the Near Wake Vortex Interactions of a Coaxial Rotor in Hover," AIAA SciTech 2020 Forum, Orlando, FL, USA, January 2020. DOI: 10.2514/6.2020-0305.

34. Kim, H. W., and Brown, R. E., "A Comparison of Coaxial and Conventional Rotor Performance," *Journal of the American Helicopter Society*, Vol. 55, (1), January 2010, pp. 12004–12004. DOI: 10.4050/JAHS.55.012004.

35. Koning, W. J., Perez, B. N. P., Cummings, H. V., Romander, E. A., and Johnson, W., "Overview of Rotor Hover Performance Capabilities at Low Reynolds Number for Mars Exploration," 50th European Rotorcraft Forum 2024, Marseille, France, September 2024.

36. Yoon, S., Lee, H. C., and Pulliam, T. H., "Computational Analysis of Multi-rotor Flows," 54th AIAA Aerospace Sciences Meeting, San Diego, CA, USA, January 2016. DOI: 10.2514/6.2016-0812.

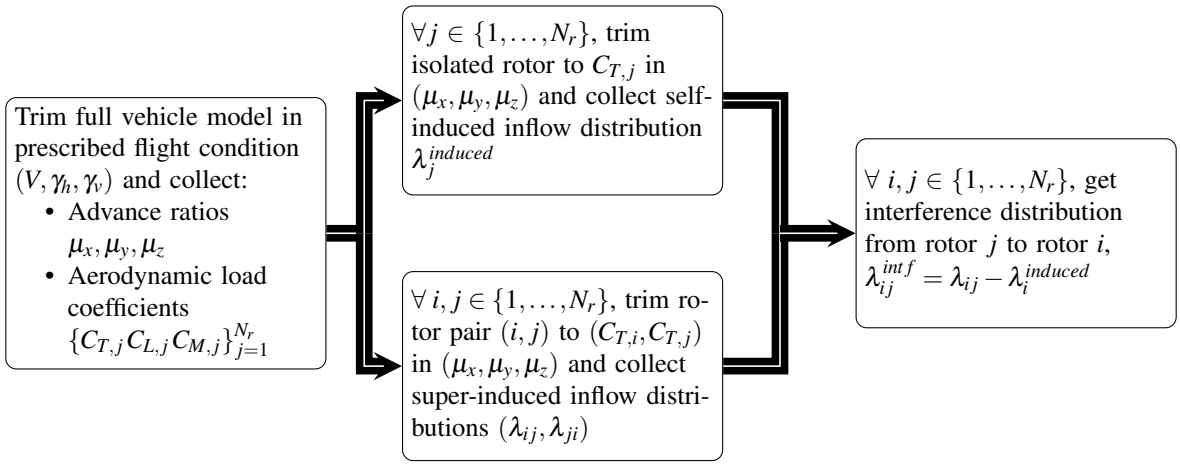

Figure 21. Flowchart for VVPM interference model data generation.

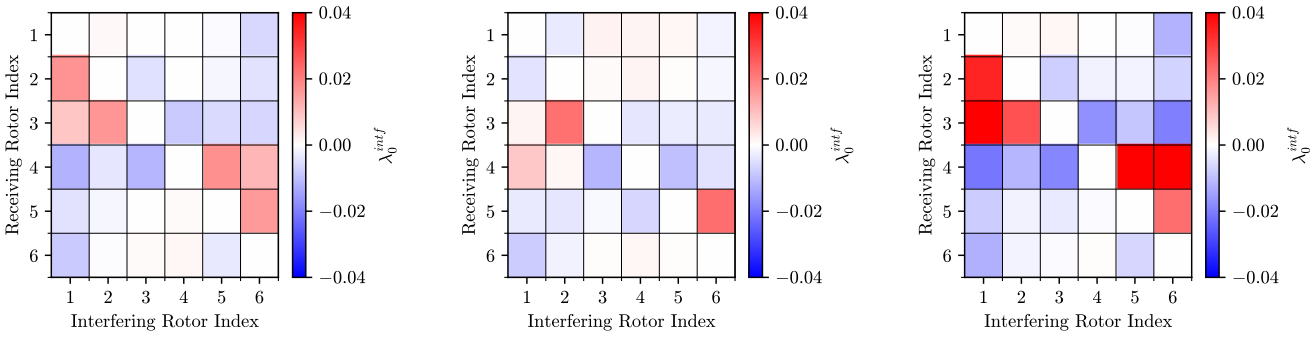

(a) $V = 50$ m/s, $\gamma_h = 0$, $\gamma_v = 0$. **(b) $V = 50$ m/s, $\gamma_h = 30$, $\gamma_v = 0$.** **(c) $V = 50$ m/s, $\gamma_h = 0$, $\gamma_v = -10$.**

Figure 22. Uniform interference components for different flight conditions.

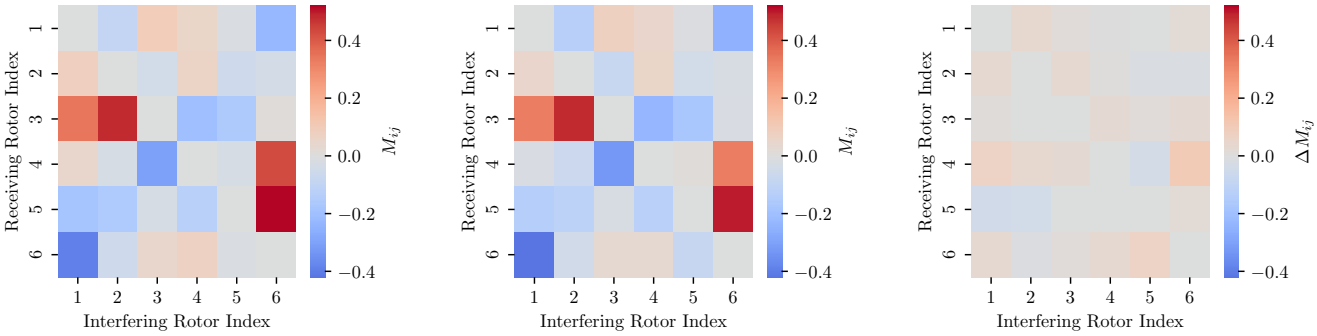

(a) True. **(b) Interpolated.** **(c) Error.**

Figure 23. Assessing interference matrix interpolation accuracy. V = 35 m/s, $\gamma_h = 10°$, $\gamma_v = 0°$